Effect of Initial Scratch on Ship Bottom Plate Corrosion Rate and Structural Crashworthiness in Grounding Incidents

Ocid MURSID[1),2)], Dean Nadhif ALFARIS[1)], Tuswan TUSWAN[1)],
Ahmad Fauzan ZAKKI[1)*], Aulia WINDYANDARI[3)], Karno R. MALAU[4)],
Haris NUBLI[5)]

[1)] *Department of Naval Architecture, Universitas Diponegoro*
Semarang, Indonesia

[2)] *Department of Naval Architecture, Ocean and Marine Engineering,*
University of Strathclyde
Glasgow, United Kingdom

[3)] *Industrial Technology Department, Vocational School, Universitas Diponegoro*
Semarang, Indonesia

[4)] *PT Limov Power Structure*
Banten, Indonesia

[5)] *University of Surrey*
Guildford, United Kingdom

*Corresponding Author e-mail: ahmadfzakki@undip.ac.id

Hitting an object in the ocean can peel off the coating on a ship's plate. The exposed plate can be vulnerable to corrosion because it is exposed to the environment and seawater, which can degrade its strength. So, the crashworthiness of the bottom plate should be evaluated in the event of a grounding incident. The ratio of the scratch area and the number of stripes are used as experimental variables. Based on seawater corrosion experiments, the plate's corrosion rate increases quadratically with the scratch area, which is then used for grounding simulations. Eighteen grounding scenarios, based on scratch size, dimensions, and corrosion exposure, reveal that only two or three stripes significantly reduce the plate's strength in simulations. In addition, in the case of two or three stripes of scratches, corrosion further reduces the plate's strength in the grounding simulations. This plate has limited space in the vertical direction, which influences the horizontal stripe of scratches and affects the plate's strength in grounding simulation, as compared to the vertical stripes. Besides this, the pattern of crack propagation depends on the reaction force.

Keywords: scratch; ship grounding; severe corrosion; finite element analysis.

1. Introduction

Based on data from the National Transportation Safety Committee (KNKT) between 2014 and 2021, approximately 6% of ship causalities are caused by grounding incidents [1]. In Europe, grounding contributed to 13% of incidents during the same period [2]. Grounding is commonly caused by a ship striking the seabed. Coating is applied to the ship's plate to protect it from corrosion, but scratches in the coating can result from several incidents, such as collision with ice and rock [3, 4]. Scratches on the ship's surface can lead to peeling of the coating and wear of the plate material. The pictorial model demonstrates that scratches on the epoxy film can expose the steel to the environment, making it easier for the paint film to lift [5]. During this exposed period, corrosion will consume the steel material [6].

Corrosion damages the ship's structure, which can lead to a decreased strength of the structure. The impact of corrosion on structural strength depends on several factors, including the type and size of the corrosion [7–12]. The bottom plate is an immersed structure, so corrosion will grow rapidly due to the composition of seawater [13–18]. On the other hand, fluid flow around immersed ship plates accelerates ship corrosion [19–22].

In grounding and collision analysis, corrosion reduces the thickness of the plate, which can degrade the strength of the structure [11, 21, 23–25]. Another research shows that pitting corrosion can also reduce crashworthiness in grounding incidents [26]. However, studies on the impact of corrosion in ship grounding and collisions remain limited. Specifically, there is a lack of research examining the detrimental effects of scratches, which, once exposed to corrosion, can compromise structural integrity during grounding scenarios. This study focuses solely on corrosion caused by thickness reduction in the scratch area, categorized as local corrosion. Therefore, this study aims to evaluate the effect of scratches on the corrosion rate and crashworthiness of the plate during a grounding incident. Chemical corrosion is used in this study to assess the corrosion rate, while, LS-Dyna simulation is employed to analyze the reaction force and crack patterns as parameters in this study.

2. Corrosion rate experimental method

2.1. Material selection and coating procedure

This study assesses the corrosion rate using SS 400 mild steel as the selected material. A detailed insight into the chemical composition of the SS 400 mild steel plate, conventionally utilized as a ship bottom plate [27], is presented in Table 1. The material preparation for the corrosion rate examination began

TABLE 1. Chemical composition of SS 400 material [27].

Element	Fe	C	Si	Mn	P	Cr	S	Cu
%	96.4	0.0337	0.193	0.288	0.0018	0.0273	0.005	0.0136

with the fabrication of specimens measuring $50 \times 50 \times 5$ mm. Seven strips of specimens were used in this study.

In the subsequent stage, each specimen was cleaned using a sandblasting procedure in accordance with the ISO 8501-1 guidelines [28]. Sandblasting was performed as a preparatory step before the application of protective coatings. Garnet abrasive material was used in this sandblasting process, with pressure maintained between 6–7 bar. To ensure consistent and accurate results, the distance between the specimen and the nozzle was kept within the range of 15–25 cm throughout the sandblasting operation. According to ISO 8501-1 [28], the blasting quality must be assessed through visual inspection to measure the SA level, as well as through roughness testing methods. The blasting procedure was conducted until each specimen reached a SA level of 2.5. Figure 1 shows a comparison of the SA levels, with the benchmark on the left side and the specimen on the right.
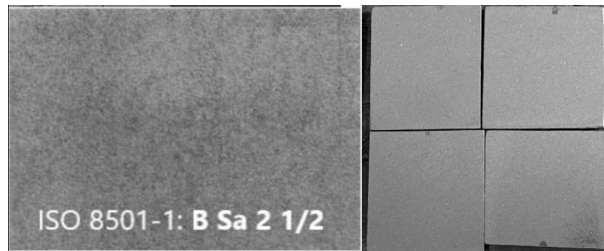

FIG. 1. Visual inspection of the material after the sandblasting process, according to ISO 8501-1 [28].

Besides the SA level, the roughness levels recorded during this investigation exhibited a marginal variation, ranging from 30 to 36 µm, as illustrated in Fig. 2. The results obtained from the roughness testing further substantiated the suitability of all examined specimens for the subsequent coating process. The consistent roughness characteristics observed throughout the sample set indicate the uniformity and effectiveness of the sandblasting treatment, ensuring a suitable surface texture for the successful application of protective coatings.

To achieve an adequate coating, it is essential to ensure that the environmental conditions meet the specified criteria, considering factors such as dew point and relative humidity. An instrument called psychrometer was employed to assess environmental and material conditions. According to the findings pre-
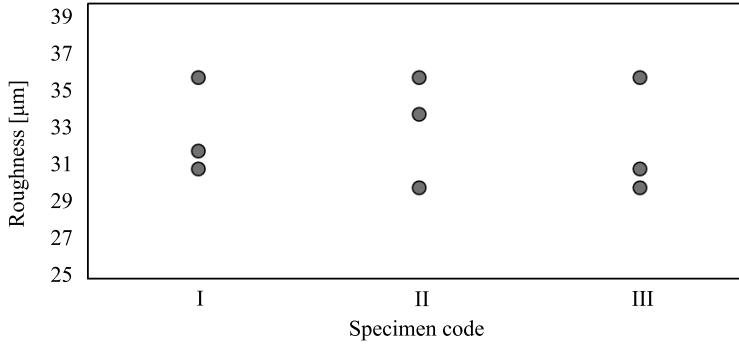
Fig. 2. Result of roughness test for different specimen codes.

sented in Table 2, the environmental conditions were suitable for the coating process, in accordance with the established criteria.

Table 2. Results of environmental conditions during the coating process.

Test criteria	Result	Criteria
Wet bulb	27°C	> 5°C
Dry bulb	31°C	> 5°C
Relative humidity	72%	< 85% RH
Plate temperature	33.6°C	> 5°C

The coating process involved referring to the material data sheet for the coating material to determine the appropriate mixing ratio and curing time. This study applied an alkyd coat to the plate using the LZI Primer type. Only the surface covered by the alkyd coat was observed, while the other surfaces were protected by a sealant. Wet film thickness (WFT) and dry film thickness (DFT) were used to assess the coating results. The LZI primer coat had an effective thickness of 55%, meaning there would be a 55% reduction in the DFT test compared to the WFT. The minimum effective coating thickness required for this study was 240 μm. Therefore, DFT measurements were used to evaluate the coating process. If a specimen did not meet the minimum DFT criteria, it was resprayed to achieve the appropriate thickness. Figure 3 presents the WFT measurement of the specimen, indicating that the minimum dry coating thickness should be 450 μm. All specimens were stored at room temperature until the coating dried completely. The results from the DFT method, obtained by multiplying the measured WTF thicknesses by 55%, are depicted in Fig. 4, revealing that the specimens met the required minimum effective thickness criteria.

All specimens were treated using a milling machine with a 5 mm spindle to create scratches on the coating surfaces. Mouth and bed scratches are the ex-
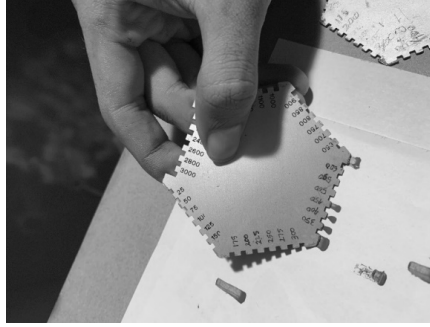
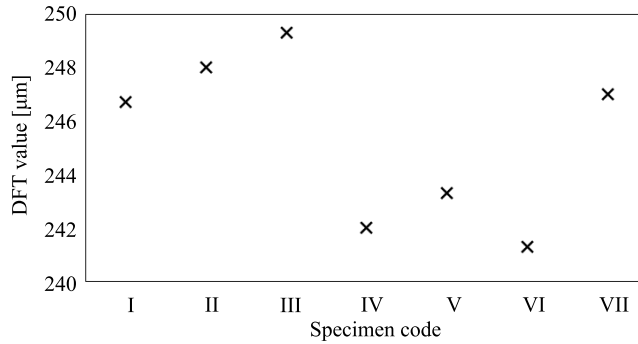Fig. 3. Example of WFT measurement results for the plain specimen.

Fig. 4. DFT measurement results for different specimen codes.

posed areas on the plate caused by the milling process. However, the milling process resulted in scratches with a depth of only 0.5 mm. Table 3 provides specifics about the specimen variables. To obtain major scratches, the scratch area ratio, which is the percentage of the scratch area to the total plate surface area (A_s/A), was set between 10–30% of the total surface area. Furthermore, specimens with

TABLE 3. Variation in scratch geometry for different specimen codes.

Specimen code	A_s/A [%]	Number of scratches	Length of scratch [mm]	Wide of scratch [mm]	Total scratch area [mm^2]
I	10	1	50	5	250
II	20	1	50	10	500
III	30	1	50	15	750
IV	10	3	16.67	5	250
V	20	3	33.34	5	500
VI	30	3	50	5	750
VII	Plain plate				

identical scratch area were differentiated by a single or triple type of scratch. The visualization of scratches in specimens is shown in Fig. 5.
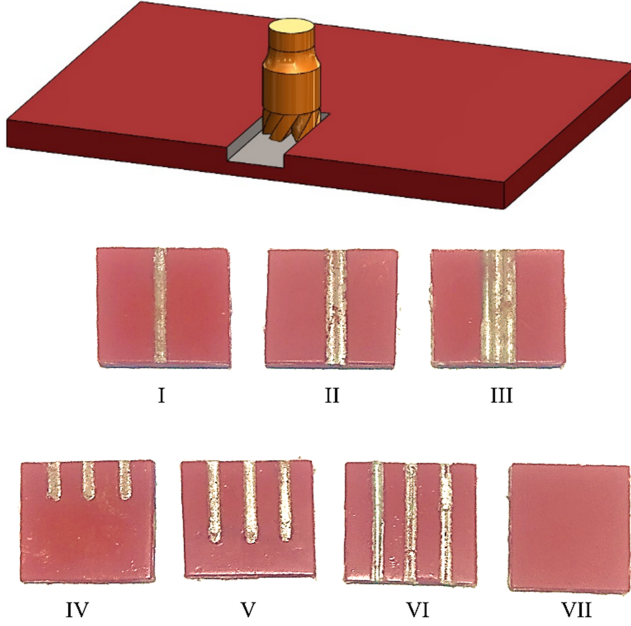

FIG. 5. Visualization of the specimen with variations in scratch size.

2.2. Procedure for corrosion rate test

The corrosion chemical test was conducted in accordance with ASTM G102 using a NaCl corrosive medium [29]. Three electrodes were used to determine the corrosion rate of the specimen. A single-channel Potentiostat Corrtest measures the corrosion rate with CS Studio 5 software. To evaluate the corrosion rate on the plate (CR) Eq. (2.1) was applied, where K_1 is equal to $3.27 \cdot 10^{-3}$ $(\mathrm{mm} \cdot \mathrm{g})/(\mu\mathrm{A} \cdot \mathrm{cm} \cdot \mathrm{yr})$, I_{corr} is the exchange current density ($\mu\mathrm{A}/\mathrm{cm}^2$), ρ is density (g/cm^3), and E_w is dimensionless of equivalent weight (for SS400 assumed to be 27.9225 g/equiv).

$$(2.1) \qquad CR = \frac{K_1 \cdot I_{\mathrm{corr}} \cdot E_w}{\rho}.$$

Table 4 presents the results of the exchange current density for SS 400 mild steel obtained through chemical corrosion testing. The corrosion rate of the plate was determined using Eq. (2.1), based on the exchange current density. This study shows that plates with triple scratches (scenarios IV, V, and VI) exhibit a slightly higher corrosion rate than those with a single scratch (scenarios I, II, and III) at the same scratch area ratio. While a triple scratch

TABLE 4. Result of corrosion rate for different scratch types.

Scenarios	I_{corr} [μA/cm^2]	Corrosion rate [mmpy]
I	283	$3.29 \cdot 10^{-2}$
II	526	$6.11 \cdot 10^{-2}$
III	672	$7.82 \cdot 10^{-2}$
IV	330	$3.84 \cdot 10^{-2}$
V	593	$6.89 \cdot 10^{-2}$
VI	721	$8.38 \cdot 10^{-2}$
VII	5.45	$6.30 \cdot 10^{-4}$

involves six mouth scratches, a single scratch has only two. As a result, the triple scratch yields a larger exposed area compared to the single scratch. However, even with similar scratch area ratios, the increase in corrosion rate varies. Interestingly, as the scratch area ratio increases, its impact on the corrosion rate diminishes, likely due to the diminishing effect of additional scratch openings on the exposed area. Calculations reveal that for scratch area ratios of 10%, 20%, and 30%, the corrosion rate increases by 17%, 13%, and 7%, respectively, when transitioning from a single to a triple scratch.

This study shows that larger scratch areas were found to lead to more critical steel corrosion, consistent with previous findings [30, 31]. The study demonstrated that larger cracks reduce the protected area, increasing the plate's susceptibility to corrosion. On the other hand, the plain plate showed almost no visible corrosion, providing evidence that the alkyd coating effectively protected the plate.

Figure 6 displays the yearly corrosion rate curve fitting based on experimental data used for grounding simulation. The regression formula yielded a qua-
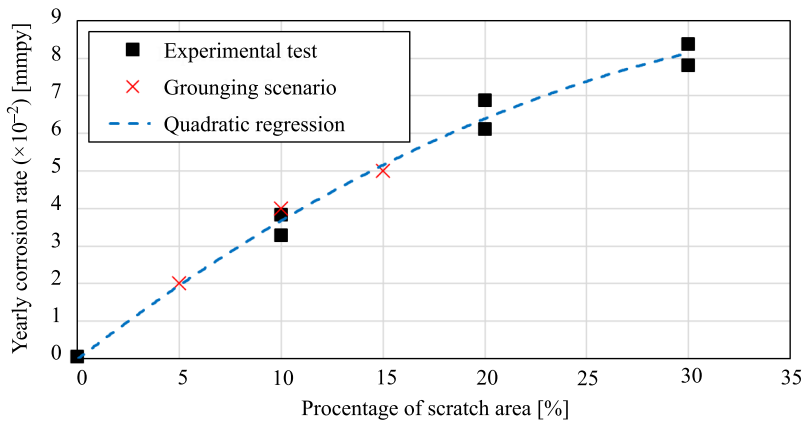

FIG. 6. Yearly corrosion rate and scratch area curve fitting between the numerical simulation results and the experimental results from FONTANA and GREENE [32].

dratic trendline. Three corrosion points, marked in red cross points at 5%, 10%, and 15%, were selected for the grounding scenario. The corrosion rates for each scenario were obtained by fitting the experimental data to the curve and rounding to the nearest number. Corrosion levels on the plate, based on the corrosion rate, were referenced from Fontana and Greene [32] for analysis. As shown in Fig. 3, the specimen with the plain plate (scenario VII) exhibited an exceptionally low corrosion rate, with the corrosion level below 0.02 mmpy. In contrast, the other specimens were categorized as having excellent corrosion resistance, with corrosion rates ranging from 0.02 to 0.1 mmpy.

3. Grounding simulation

3.1. Material model

SS400 steel was used to determine the corrosion rate in the corrosion experimental test. However, for the LS-DYNA grounding simulation, only S235 steel was used, as its mechanical properties are readily available in the software. Both SS400 and S235 are commonly used in structural applications such as building frames, bridges, and construction projects due to their good weldability and low carbon content, which reduces the risk of weld cracking. The primary distinctions between the two materials lie in their specific standards and slight variations in chemical composition and mechanical properties. S235 generally has a lower carbon content, limited to 0.17%, slightly affecting material selection based on regional standards and engineering requirements. Several studies adopted S235 steel mechanical properties for grounding simulation using an isotropic-kinematic hardening material model [33–35]. This isotropic-kinematic material model is widely used in ship grounding and failure simulations and is readily available in LS-DYNA. In the grounding simulation, a $1200 \times 720 \times 5$ mm

Table 5. Material properties of S235 steel grade.

Material properties	Value	Unit
Density (ρ)	7850	kg/m^3
Young's modulus (E)	210	GPa
Poisson's ratio (υ)	0.3	–
Yield stress (σ_0)	235	MPa
Tangent modulus (E_{tan})	672	MPa
Beta (β)	0.225	–
Strain rate constant (C)	500	s^{-1}
Material constant (p)	5	–
Strain failure predefined ($\varepsilon_p^{\text{fail}}$)	0.35	–

sample from the Alsos and Amdahl experiment [36] was used to evaluate bottom strength. Structural steel S235 from the Alsos and Amdahl experiment [36] was also used for model validation.

Cowper and Symonds developed the Cowper–Symonds (CS) model [37] to evaluate the quasi-static yield stress (σ_y^s) and dynamic flow stress (σ_y^d) in terms of uniaxial effective plastic strain (ε) and strain rate ($\dot{\varepsilon}$). The flow stress for the isothermal condition in the CS model is formulated in Eq. (3.1).

$$(3.1) \qquad \sigma_y(\varepsilon, \dot{\varepsilon}) = \sigma_y^s(\varepsilon) \left(1 + \left(\frac{\dot{\varepsilon}}{C} \right)^{\frac{1}{p}} \right),$$

where C and p are material parameters selected to describe the material's sensitivity to strain rate. The quasi-static yield stress σ_y^s is explained by the power lawin Eq. (3.2):

$$(3.2) \qquad \sigma_y(\varepsilon, \dot{\varepsilon}) = K(\varepsilon + \varepsilon_0)^n,$$

where $\varepsilon_0 = \left(\frac{E}{K} \right)^{\frac{1}{(n-1)}}$, K is the strength hardening coefficient, n is the strength hardening exponent, and E is Young's modulus. With Eq. (3.2), Eq. (3.3) becomes:

$$(3.3) \qquad \sigma_y(\varepsilon, \dot{\varepsilon}) = K \left[\varepsilon + \left(\frac{E}{K} \right)^{\frac{1}{(n-1)}} \right]^n \left[1 + \left(\frac{\dot{\varepsilon}}{C} \right)^{\frac{1}{p}} \right].$$

This study uses a strain failure criterion as a parameter for assessing structural damage, as shown in Eq. (3.4). Material failure occurs when the plastic strain of the material reaches the predefined strain failure limit:

$$(3.4) \qquad \varepsilon_p \geq \varepsilon_p^{\text{fail}}.$$

3.2. Model of artificial scratch geometry

The initial scratch on the plate exhibits a random pattern. To standardize the experimental set up, an artificial scratch was created in a rectangular area, as shown in Fig. 7. Scratches on the plate can peel off the steel coating, and in the worst case, they can wear down the steel plate [38]. So, in this study, the artificial scratch was given a depth of 0.5 mm. Six different artificial scratches were created, shown in Fig. 7. In Fig. 7, scenarios B, C, E, and F have scratches positioned a 200 mm away from the plate edge. MURSID *et al.* [26] used a 200 mm pitch in their grounding simulation of a $1200 \times 720 \times 5$ mm plate. The scratch widths of 60 mm and 36 mm represent 5% of the ratio of scratch to plate area.
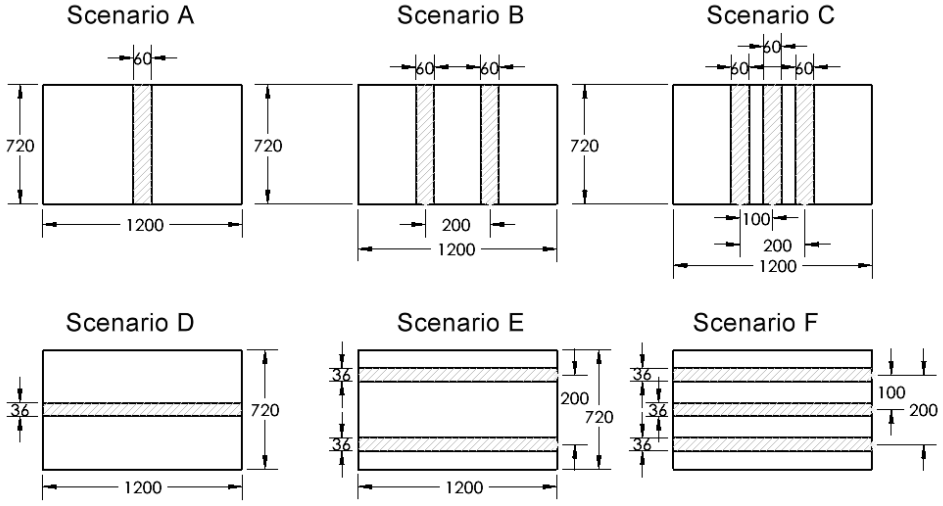
FIG. 7. Six different scenarios of scratch geometry.

The precise dimensions of the six initial scratches in this simulation are de-
picted in Fig. 7. Each scenario was subdivided into three conditions: the initial
state and exposures of 5 and 10 years to seawater. Consequently, a total of 18 sce-
narios were utilized in the grounding simulation. As indicated by Fig. 8, a scratch
of 0.5 mm was introduced on the plate's surface in the initial condition. Over an
extended period of exposure to the environment, the scratched portion of the
plate underwent corrosion, while the coated surface remained unaffected. In this
study, corrosion only affects the scratched bed, while the scratch in the mouth
is neglected. Accordingly, the width of the scratch remains unchanged following
the corrosion effect. Corrosion consumes steel in a random and uneven man-
ner. Therefore, the corroded plate was refined for the grounding simulation to
establish an ideal geometry for finite element modeling. Upon analyzing the re-
fined geometry, it became evident that corrosion occurred orthogonally to the
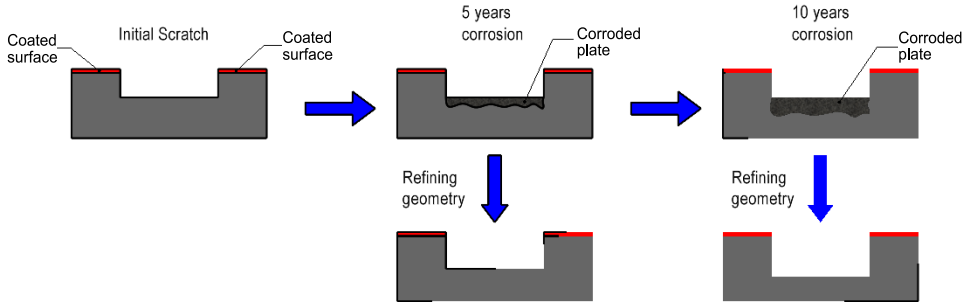surface of the plate, resulting in a consistent width of the corroded scratch.

FIG. 8. Schematic diagram of material lost due to corrosion process.

The corrosion growth in this simulation was conducted based on the experimental corrosion test results shown in Fig. 6. The test showed that at 5%, 10%, and 15% scratch areas, the corresponding corrosion rates were 0.02 mmpy, 0.04 mmpy, and 0.05 mmpy, respectively. To find the scratch depth (d) in the grounding simulation, Eq. (3.5) was used. Here, T_y represents the exposed period of the bottom plate in years, d_0 is the initial depth of the scratch, and CR is the corrosion rate. The resulting scratch depths in the grounding simulation are shown in Table 6.

$$(3.5) \qquad\qquad d = d_0 + CR \cdot T_y.$$

TABLE 6. Grounding scenarios.

Scenario codes	A_s/A [%]	CR [mmpy]	T_y [years]	d [mm]
A0	5	0.02	0	0.5
A5	5	0.02	5	0.6
A10	5	0.02	10	0.7
B0	10	0.04	0	0.5
B5	10	0.04	5	0.7
B10	10	0.04	10	0.9
C0	15	0.05	0	0.5
C5	15	0.05	5	0.75
C10	15	0.05	10	1.0
D0	5	0.02	0	0.5
D5	5	0.02	5	0.6
D10	5	0.02	10	0.7
E0	10	0.04	0	0.5
E5	10	0.04	5	0.7
E10	10	0.04	10	0.9
F0	15	0.05	0	0.5
F5	15	0.05	5	0.75
F10	15	0.05	10	1.0

3.3. Boundary condition and applied load

Figure 9 shows the boundary conditions for this simulation. The grounding incident boundary conditions are modeled similarly to those in the study by Mursid *et al.* [26], which were based on experimental results from Alsos and Amdahl [36]. An indenter penetrates the plate in the orthogonal direction, while the plate is fixed along all edges. The ship scratch position is on the outer plate of the ship bottom so that this scratch faces directly toward the indenter.

In previous studies, various indenter shapes have been used to represent seabed conditions, with spherical impactors being the most common to simulate the effect of a rock [36, 39–43]. Additionally, the material used in this simulation, as well as in the Alsos experiment, is S235 steel.
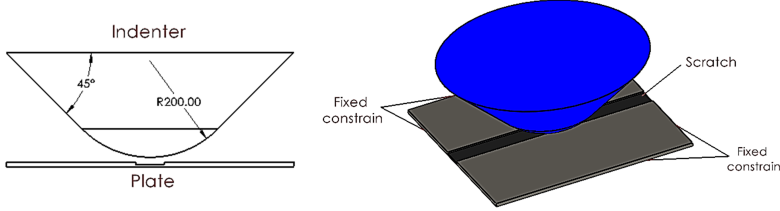

FIG. 9. Boundary condition of grounding simulation.

An 8-node solid element was used in the modeling of the ship groundings simulation. A 3D solid element was needed to capture the failure phenomenon in the plate impacted by the circular indenter. The node position in the hexahedron element is defined by Eq. (3.4) [44]. For comparison, Φ_j, a shape function for 8-node hexahedron elements, is calculated in Eq. (3.5). Equations (3.4) and (3.5) are used to compute node displacements in this simulation, which models a grounding incident. On the other hand, the indenter is described as a rigid element in this simulation, where stress-strain calculations are neglected in the elements due to its rigid nature.

$$(3.6) \qquad x_i(x_a, t) = x_i\big(x_a(\xi, \eta, \zeta)t\big) = \sum_{k=0}^{n} \Phi_j(\xi, \eta, \zeta) x_i^j(t),$$

$$(3.7) \qquad \Phi_j = \frac{1}{8}(1 + \xi\xi_j)(1 + \eta\eta_j)(1 + \zeta\zeta_j).$$

3.4. Validation test between numerical and experimental tests

The LS-Dyna simulation employed in this study was validated with data from the ALSOS and AMDAHL experiment [36]. A plain plate was utilized for the validation of the numerical methods. This validation approach was previously used by MURSID *et al.* [26], as depicted in Fig. 10. Figure 10 demonstrates a striking similarity in the patterns of increasing reaction force with indenter penetration between the experimental and numerical results. Moreover, it was observed that the plate experienced failure near 200 mm of indenter penetration. The validation results show that the error between the numerical simulation and Alsos and Amdahl experimental data is within acceptable limits, with a maximum reaction force error of 5.8% and a maximum penetration error of 7.89%. These errors are considered acceptable for the purpose of this study. To fur-
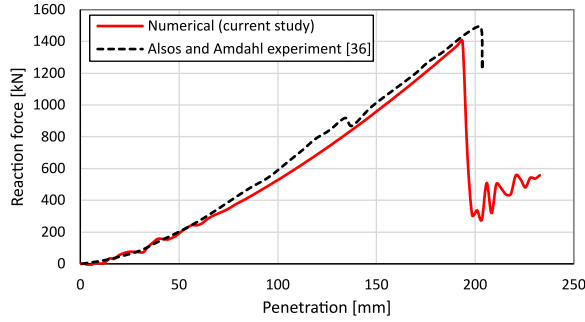
FIG. 10. Validation test between the current numerical simulation and the ALSOS and AMDAHL experiment [36].

ther support this validation, the damaged contour of the plain plate exhibited similar patterns in both experimental and simulations results, as illustrated in Fig. 11. This reveals that the location of the crack in both the experimental and simulated results was found on the narrow sides of the plate.
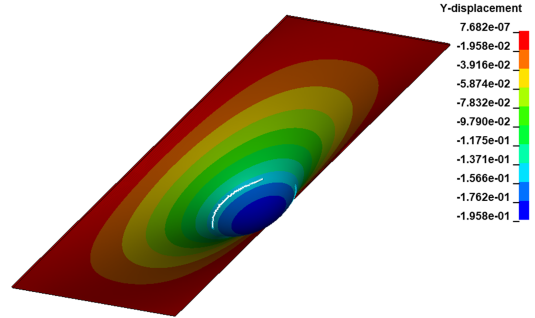
a)   b)

FIG. 11. Crack displacement in the grounding simulation:
a) ALSOS and AMDAHL experiment [36], b) numerical simulation.

4. RESULT AND DISCUSSION

The reaction force analysis is crucial in collision and grounding incidents due to its direct correlation with kinetic energy. Kinetic energy is an integral factor in these simulations, representing the cumulative effect of reaction force on the displacement of penetration. Higher kinetic energy values in the simulation indicate that more resistance is required to induce structural failure. On the other hand, a decline in reaction force during the grounding incident suggests the initiation of crack nucleation. Investigating reaction force and kinetic energy in the plain plate serves as a benchmark test to assess the impact of scratches and corrosion. Examining various scenarios, as illustrated in Figs. 12 and 13,
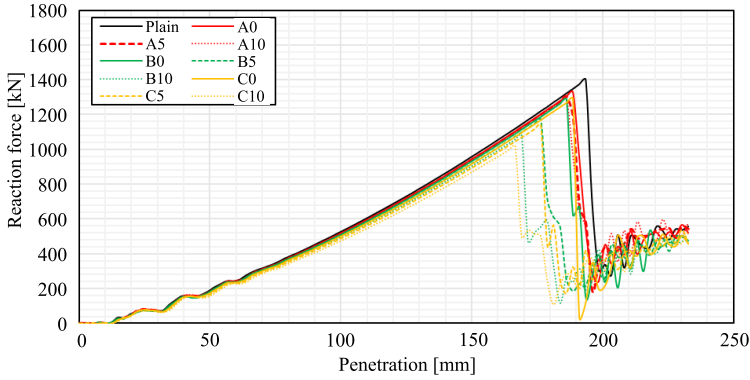
FIG. 12. Comparison of the reaction force in all grounding simulation scenarios.
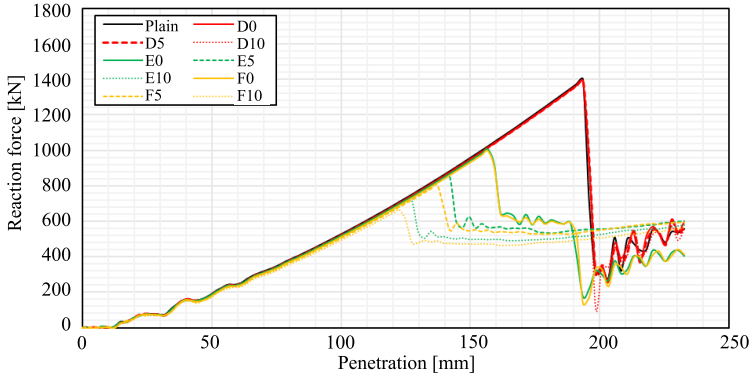

FIG. 13. Reaction force in the grounding simulation for the plain plate, scenarios D, E, and F.

demonstrates a consistent increase in reaction force across all cases, indicating that a plate with an early crack requires less energy to propagate the crack. The observed drop in reaction force during the grounding incident further supports the initiation of crack nucleation.

Figure 12 shows the reaction force during the grounding incident for the plain plate scenarios A, B, and C. It is evident that a single strip of scratch (scenario A) has small effect on the grounding incident compared to the plain plate. The corrosion effect does not significantly influence the maximum reaction force. The insignificant decrease in reaction force influences the kinetic energy required to break the plate, as shown in Fig. 14. Reaction force and kinetic energy in scenarios B0 and C0 are similar to scenario A. Additionally, the occurrence of double and triple scratch strip corrosion (scenarios B5, B10, C5, and C10) suggests a compromised (reduced) plate strength. The structure consistently demonstrates similar reaction force and kinetic energy values across all initial conditions and exposure periods.
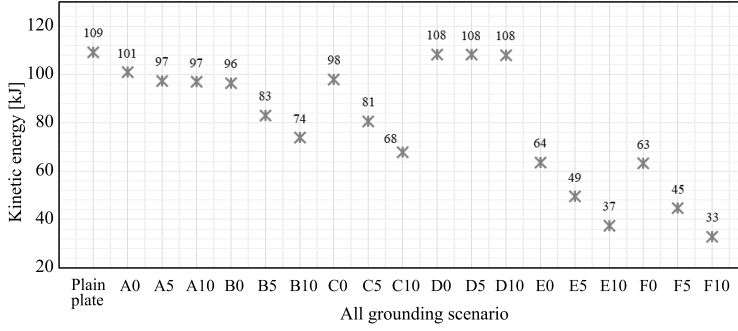
FIG. 14. Comparison of the kinetic energy across all grounding scenarios.

Figure 13 shows the reaction force in the plain plate and horizontal scratch stripe (scenarios D, E, and F). The reaction force for a single horizontal (scenario D) is comparable to a single vertical stripe (scenario A), which proves that a single stripe scratch in the middle plate has little influence in both vertical and horizontal directions. Figure 14 and Table 7 show the effect of scratches and ex-

TABLE 7. Reduction percentage of kinetic energy.

Grounding scenario	Kinetic energy [kJ]	Reduction percentage of kinetic energy [%]
Plain	109	–
A0	101	8
A5	97	12
A10	97	12
B0	96	13
B5	83	26
B10	74	35
C0	98	11
C5	81	28
C10	68	41
D0	108	1
D5	108	1
D10	108	1
E0	64	45
E5	49	60
E10	37	72
F0	63	46
F5	45	64
F10	33	76

posure time on the strength of the structure, measured by kinetic energy. The kinetic energy in scenario D is higher than in scenario A. However, the presence of two and three horizontal stripes (scenarios E and F) influences the reaction force pattern. With each additional year of exposure, scenarios E and F have similar reaction force values, i.e., they decrease consistently. The kinetic energy in scenarios E and F decreases drastically over time. In the worst scenario (scenario F10), kinetic energy is reduced to one-third of the plain plate's kinetic energy. Based on these kinetic energy parameters, this indicates that a 1 mm depth in the scratch area can reduce the plate's strength by almost 70%.

A perfect circular crack emanates from a single strip of scratch, represented in the plain plate, scenarios A0, A5, A10, D0, D5, and D10. Circular cracks can be predicted by circular stress hotspots, as shown in Fig. 15. In the next step, the crack initiates on the narrow side of the plate near the contact point, as seen in Fig. 16, and then spreads to the other side in a circular pattern, as seen in Fig. 17. Scenarios A and D show the effect of a single stripe on crack geometry, where the crack can be neglected, similar to the plain plate.

Scenarios B, C, E0, and F0 show a crack pattern similar to that of a riser clamp. Figure 15 shows that the hotspot stress can appear as a circular pattern or a couple of crescents, forming a crack pattern like that of a riser clamp. Shortly thereafter, a crack initiates on the wider side in scenarios B and C, caused by a couple of stripes beside the contact point. These stripes shift the weakest point of stress from the narrow side to the wider side (see Fig. 16). On the other hand, Fig. 16 shows that in scenarios E0 and F0, the crack initiates on the narrow side because of a couple of scratches in this position. This suggests that scenarios B, C, E0, and F0 are weak points on the plate. Figure 17 shows how the crack propagates in an arc pattern, and when it meets the scratch side, it deflects to become a straight crack.

In scenarios E5, E10, F5, and F10, Fig. 14 shows that the stress hotspot is in the center of several scratches. Crack nucleation on the narrow side can be seen in Fig. 15. Then, the crack propagates in a straight line, following the scratch stripes, as shown in Fig. 16. A deeper scratch is needed to create a collateral crack, which does not occur in scenarios E0 and F0.

The results indicate that certain factors influence the final form of cracks in the grounding simulation. Specifically, these factors are area ratio, depth, and position of the scratch. Furthermore, the findings align with previous studies on the same or similar topics, validating or supporting the conclusions of earlier research. Several studies have shown that circular indenters in impact simulation will cause plate fracture, in a circumference pattern at the contact point [26, 45–47]. On the other hand, a study on the effect of local corrosion, particularly pitting corrosion, shows that local corrosion can alter crack and failure modes [26]. Furthermore, studies on plates with local corrosion subjected to
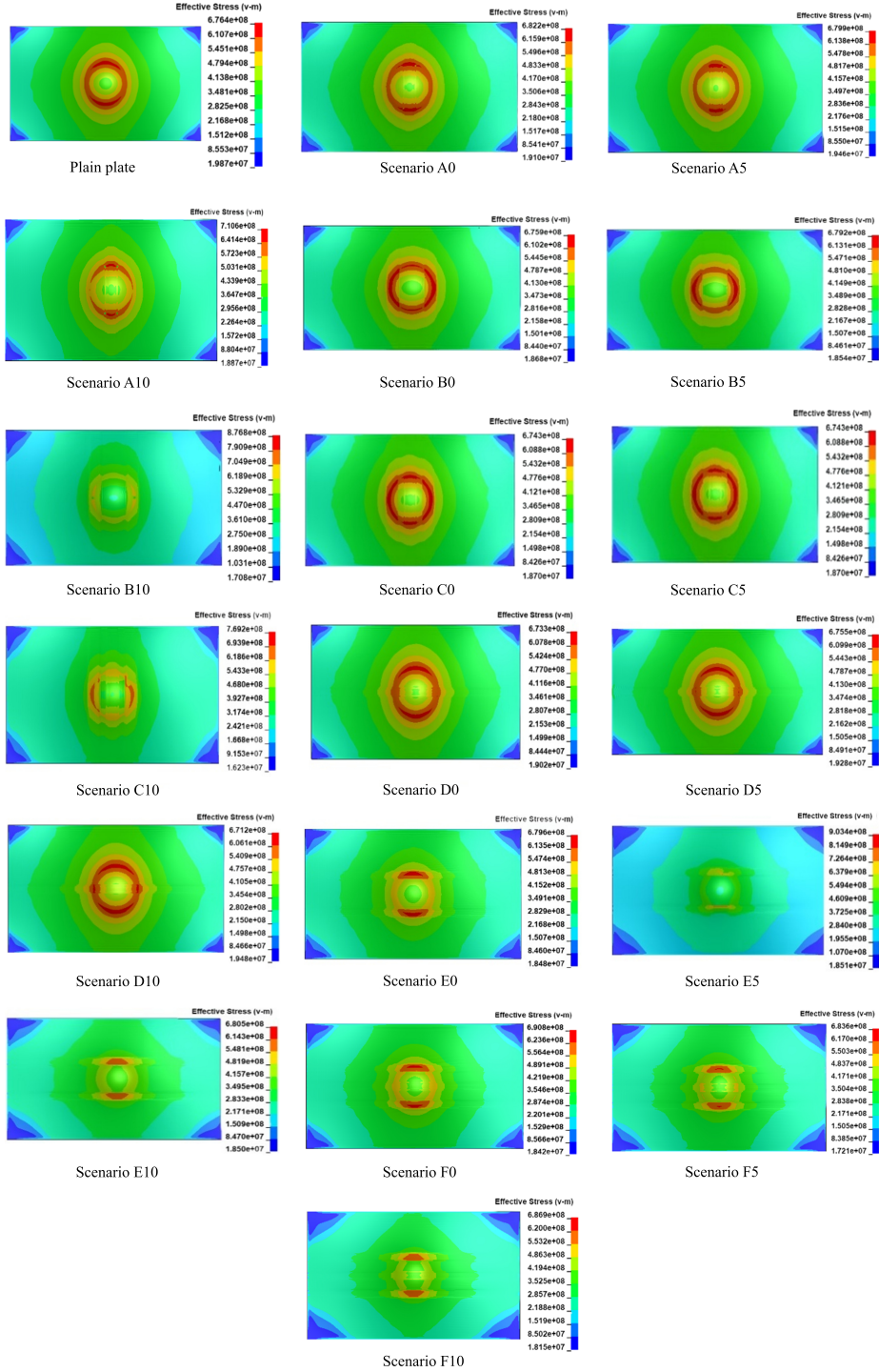
Fig. 15. Hotspot stress before crack nucleation at all grounding scenarios.

Plain plate

Scenario A0

Scenario A5

Scenario A10

Scenario B0

Scenario B5

Scenario B10

Scenario C0

Scenario C5

Scenario C10

Scenario D0

Scenario D5

Scenario D10

Scenario E0

Scenario E5

Scenario E10

Scenario F0

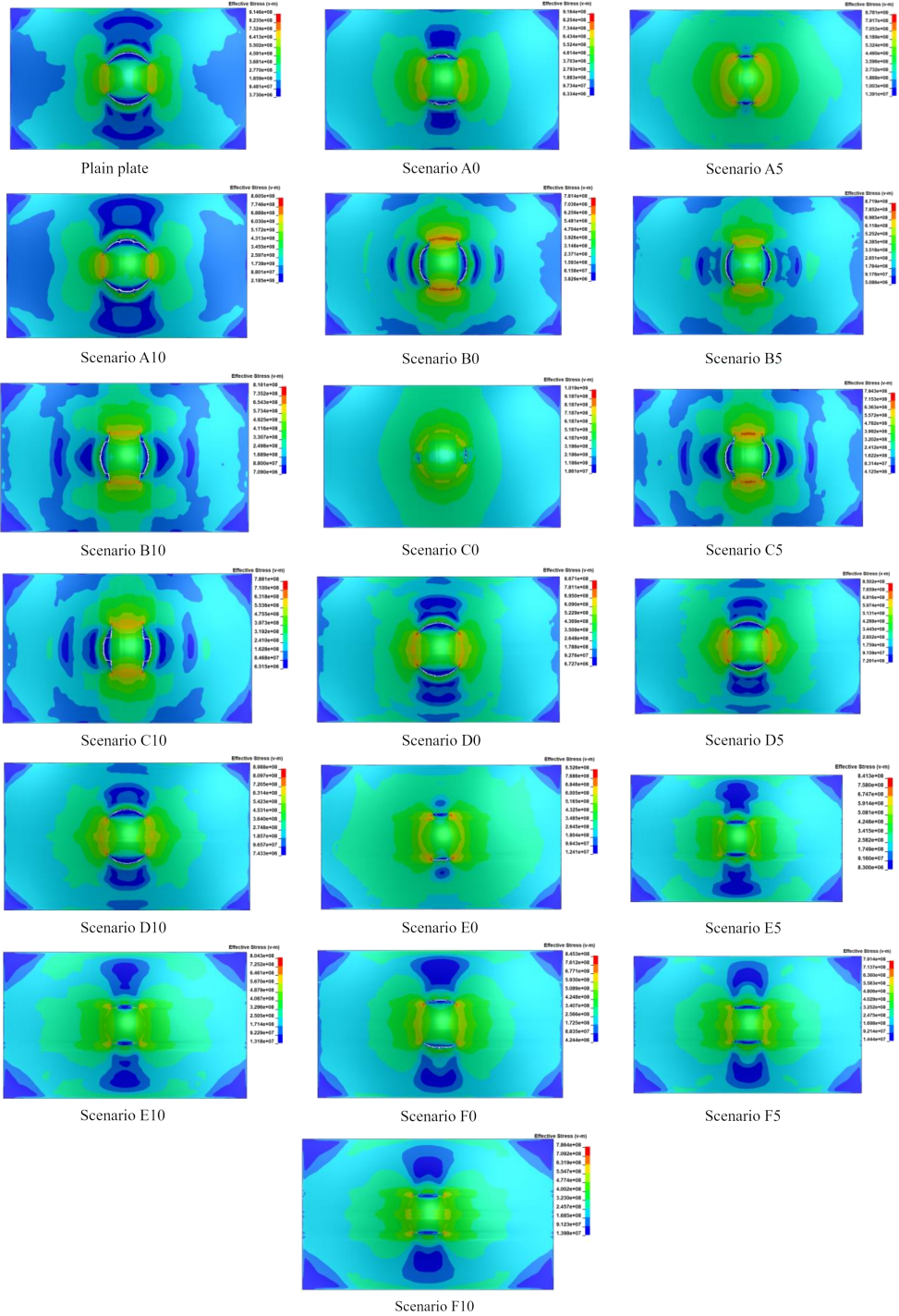Scenario F5

Scenario F10

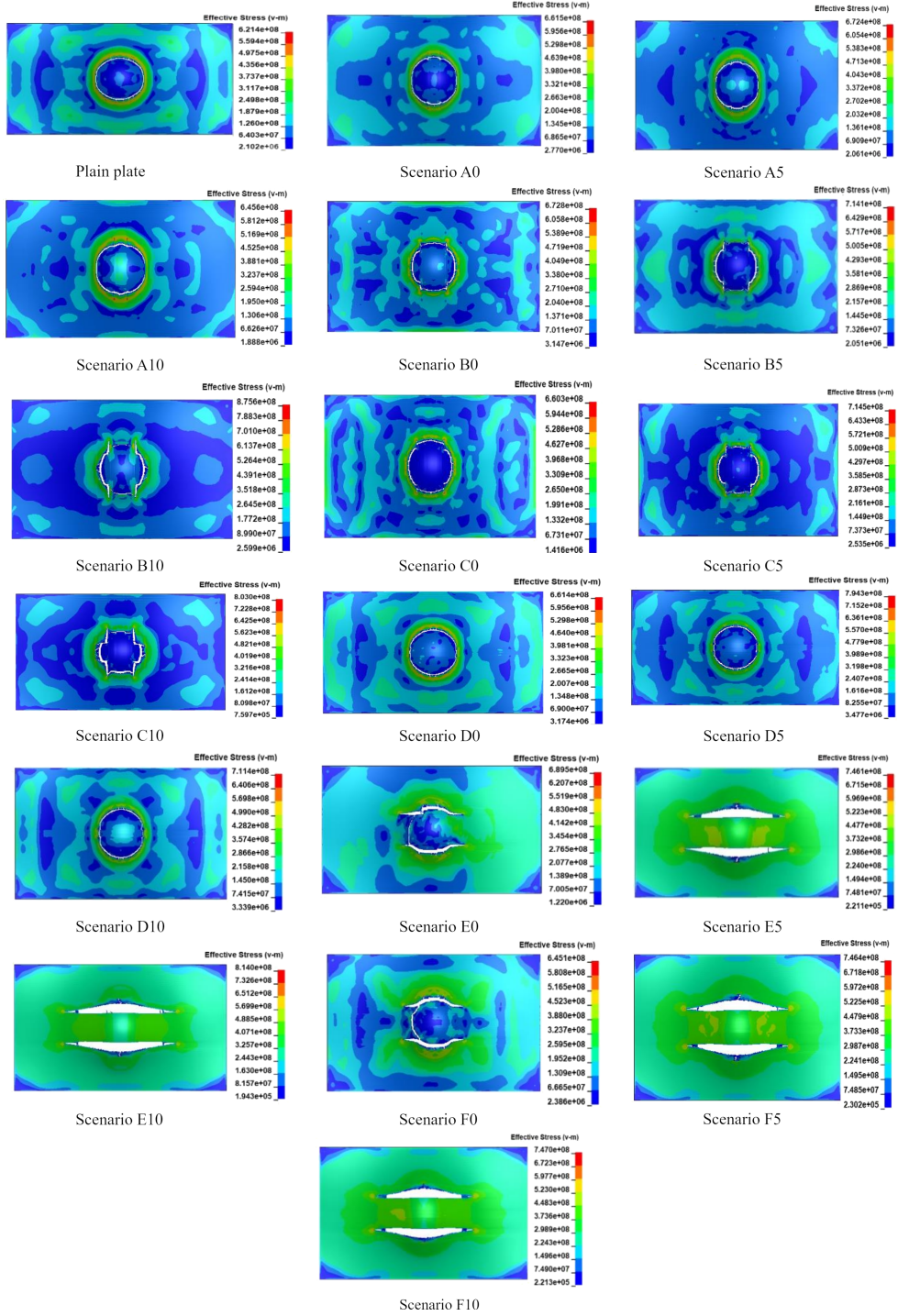Fig. 16. Crack initiation at all grounding scenarios.

Fig. 17. Crack propagation at all grounding scenarios.

axial compression and tension, indicate that several corrosion conditions can change crack initiation and propagation [48–50].

5. Conclusion

In this study, an experimental corrosion test was conducted to investigate the effect of scratches on the corrosion rate. Variations in the corrosion experiment involved changes in the scratch ratio and the number of scratch stripes. Based on experiments' results, it was observed that an increase in the scratch ratio percentage led to an increase in the corrosion rate, following a quadratic function. Plates with three stripes showed a slightly higher corrosion rate compared to those with a single stripe. The corrosion rate data obtained from the experimental tests were then regressed for application in the grounding simulation.

The grounding simulation in this study was performed in 18 different scenarios. The simulation results from the plain plate were validated against the Alsos and Amdahl experiment, confirming that the boundary conditions and simulation settings were appropriate. A correlation was observed between the reaction force and crack patterns in the plate. Circular cracks required more energy to initiate, followed by riser clamp-like cracks and straight cracks. The study found that crack nucleation occurred earlier in plates with two or three stripes than those with a single stripe. Additionally, plates with two or three stripes exposed to seawater for longer periods exhibited weaker performance during grounding incidents.

Based on this study, scratches on the ship's surface strip away its protective coating, accelerating corrosion on the affected plates. This phenomenon significantly reduces the ship's structural strength, particularly during grounding incidents. Prolonged exposure of these scratches to corrosive environments can lead to a drastic decrease in strength over time. However, since scratches on the ship's bottom are difficult to inspect, the need for regular detection of potential damage to ship plates is crucial. While this study, focused on grounding conditions, future research could explore the effects of corrosion due to scratches in other scenarios, such as hull girder strength, collisions, fatigue, and other structural integrity concerns.

Funding

Competing interests

The authors declare no competing interest.

References

1. KNKT, *Maritime Investigation Reports*, n.d. http://knkt.dephub.go.id/knkt/ntsc_mari time/maritime_investigation_report1.htm (accessed September 16, 2022).

2. EMSA, *Annual Overview of Marine Casualties and Incidents 2021*, European Maritime Safety Agency Lisbon, 2022, https://safety4sea.com/emsa-annual-overview-of-marine-casualties-and-incidents-2022/ (accessed May 23, 2023).

3. PINEAU J.-P., LE SOURNE H., A simplified approach to assess the resistance of a ship sliding on elliptic paraboloid rock, *Marine Structures*, **83**: 103151, 2022, https://doi.org/10.1016/j.marstruc.2021.103151.

4. ZHANG J., LIU Z., ONG M.C., TANG W., Numerical simulations of the sliding impact between an ice floe and a ship hull structure in ABAQUS, *Engineering Structures*, **273**: 115057, 2022, https://doi.org/10.1016/j.engstruct.2022.115057.

5. BALUSAMY T., NISHIMURA T., In-situ monitoring of local corrosion process of scratched epoxy coated carbon steel in simulated pore solution containing varying percentage of chloride ions by localized electrochemical impedance spectroscopy, *Electrochimica Acta*, **199**: 305–313, 2016, https://doi.org/10.1016/j.electacta.2016.02.034.

6. JIA X., SONG J., QU X., CAO F., JIANG B., ATRENS A., PAN F., Effect of scratch on corrosion resistance of calciumphosphate conversioncoated AZ80 magnesium alloy, *Transactions of Nonferrous Metals Society of China*, **32**(1): 147–161, 2022, https://doi.org/10.1016/S1003-6326(21)65784-9.

7. KIM C., OTERKUS S., OTERKUS E., KIM Y., Probabilistic ship corrosion wastage model with Bayesian inference, *Ocean Engineering*, **246**: 110571, 2022, https://doi.org/10.1016/j.oceaneng.2022.110571.

8. QIU F., WANG H., QIAN H., HU H., JIN X., FAN F., Evaluation of compressive properties of the ship plate after seawater corrosion based on 3D evolution prediction, *Ocean Engineering*, **266**: 112561, 2022, https://doi.org/10.1016/j.oceaneng.2022.112561.

9. FENG L., LI D., SHI H., ZHANG Q., WANG S., A study on the ultimate strength of ship plate with coupled corrosion and crack damage, *Ocean Engineering*, **200**: 106950, 2020, https://doi.org/10.1016/j.oceaneng.2020.106950.

10. KIM D.K., PARK D.K., KIM H.B., SEO J.K., KIM B.J., PAIK J.K., KIM M.S., The necessity of applying the common corrosion addition rule to container ships in terms of ultimate longitudinal strength, *Ocean Engineering*, **49**: 43–55, 2012, https://doi.org/10.1016/j.oceaneng.2012.04.012.

11. LIU B., GARBATOV Y., ZHU L., GUEDES SOARES C., Numerical assessment of the structural crashworthiness of corroded ship hulls in stranding, *Ocean Engineering*, **170**: 276–285, 2018, https://doi.org/10.1016/j.oceaneng.2018.10.034.

12. SHIFLER D.A., Corrosion performance and testing of materials in marine environments, [in:] *Corrosion in Marine and Saltwater Environtments II. Proceedings of the International Symposium*, D.A. Shifler, T. Tsuru, P.M. Natishan, S. Ito [Eds.], Proceedings Volume 2004-14, pp. 1–12, The Electrocemical Society, Inc., Pennington, NJ, 2005.

13. MELCHERS R.E., Probabilistic models for corrosion in structural reliability assessment – Part 2: Models based on mechanics, *Journal of Offshore Mechanics and Arctic Engineering*,**125**(4): 272–280, 2003, https://doi.org/10.1115/1.1600468.

14. DAVIS J.R. [Ed.], *Metal Handbook. Vol. 13: Corrosion*, ASM International, 1987.

15. MELCHERS R.E., Effect of immersion depth on marine corrosion of mild steel, *Corrosion*, **61**(9): 895–906, 2005, https://doi.org/10.5006/1.3280659.

16. LAQUE F.L., *Marine Corrosion: Causes and Prevention*, New York: Wiley 1975.

17. MERCER A.D., LUMBARD E.A., Corrosion of mild steel in water, *British Corrosion Journal*, **30**(1): 43–55, 1995, https://doi.org/10.1179/000705995798114177.

18. WOLOSZYK K., GARBATOV Y., KOWALSKI J., SAMSON L., Experimental and numerical investigations of ultimate strength of imperfect stiffened plates of different slenderness, *Polish Maritime Research*, **27**(4): 120–129, 2020, https://doi.org/10.2478/pomr-2020-0072.

19. XIA J., LI Z., JIANG J., WANG X., ZHANG X., Effect of flow rates on erosion corrosion behavior of hull steel in real seawater, *International Journal of Electrochemical Science*, **16**(5): 210532, 2021, https://doi.org/10.20964/2021.05.60.

20. LIU Y., LIU H., Prediction of corrosion rates of a ship under the flow accelerated corrosion mechanism, *Corrosion Reviews*, **39**(5): 445–452, 2021, https://doi.org/10.1515/corrrev-2021-0018.

21. FERRY M., WAN NIK W.B., MOHD NOOR C.W., The influence of seawater velocity to the corrosion rate and paint degradation at mild steel plate immersed in sea water, *Applied Mechanics and Materials*, **554**: 218–221, 2014, https://doi.org/10.4028/www.scientific.net/AMM.554.218.

22. SHEHADEH M., HASSAN I., Study of sacrificial cathodic protection on marine structures in sea and fresh water in relation to flow conditions, *Ships and Offshore Structures*, **8**(1): 102–110, 2013, https://doi.org/10.1080/17445302.2011.590694.

23. RINGSBERG J.W., LI Z., JOHNSON E., KUZNECOVS A., SHAFIEISABET R., Reduction in ultimate strength capacity of corroded ships involved in collision accidents, *Ships and Offshore Structures*, **13**(Sup 1): 155–66, 2018, https://doi.org/10.1080/17445302.2018.1429158.

24. BAXEVANIS D., *Residual Strength Assessment of Corroded Ships Involved in Ships-to-Ship Collisions*, Master's Thesis, Chalmers University of Technology, 2019.

25. LIU B., ZHU L., CHEN L., Numerical assessment of the resistance of ship double-hull structures in stranding, [in:] *Progress in the Analysis and Design of Marine Structures, Proceedings of the 6th International Conference on Marine Structures (MARSTRUCT 2017), May 8–10, 2017, Lisbon, Portugal*, C. Guedes Soares, Y. Garbatov [Eds.], pp. 469–476, CRC Press, 2017, https://doi.org/10.1201/9781315157368-60.

26. MURSID O., TUSWAN T., SAMUEL S., TRIMULYONO A., YUDO H., HUDA N., NUBLI H., PRABOWO A.R., Effect of pitting corrosion position to the strength of ship bottom plate in grounding incident, *Curved and Layered Structures*, **10**(1): 20220199, 2023, https://doi.org/10.1515/cls-2022-0199.

27. SUROJO E., ANINDITO J., PAUNDRA F., PRABOWO A.R., BUDIANA E.P., MUHAYAT N., BADARUDDIN M., TRIYONO, Effect of water flow and depth on fatigue crack growth rate of underwater wet welded low carbon steel SS400, *Open Engineering*, **11**(1): 329–338, 2021, https://doi.org/10.1515/eng-2021-0036.

28. ISO 8501-1, *Preparation of Steel Substrates Before Application of Paints and Related 29 Products—Visual Assessment of Surface Cleanliness—Part 1: Rust Grades and 30 Preparation Grades of Un-coated Steel Substrates and of Steel Substrates After Overall 31 Removal of Previous Coatings*, ISO Geneva, Switzerland, 2007.

29. ASTM, *Standard Practice for Calculation of Corrosion Rates and Related Information from 33 Electrochemical Measurements, G102-89*, ASTM International, West Conshohocken, USA, 2004.

30. WU B., MING H., ZHANG Z., MENG F., LI Y., WANG J., HAN E.-H., Effect of surface scratch depth on microstructure change and stress corrosion cracking behavior of alloy 690TT steam generator tube, *Corrosion Science*, **192**: 109792, 2021, https://doi.org/10.1016/j.corsci.2021.109792.

31. XIONG Z., WANG Y., YANG B., WANG Y., Stress corrosion cracking of 316LN stainless steel with orthogonal scratches, *Journal of Materials Research and Technology*, **24**: 10040–10052, 2023, https://doi.org/10.1016/j.jmrt.2023.02.205.

32. FONTANA M.G., GREEN N.D., *Corrosion Engineering*, 3rd ed., McGraw-Hill Education, 1985.

33. NIKLAS K., BERA A., The influence of selected strain-based failure criteria on ship structure damage resulting from a collision with an offshore wind turbine monopile, *Polish Maritime Research*, **28**(4): 42–52, 2021, https://doi.org/10.2478/pomr-2021-0048.

34. DNVGL, *Determination of structural capacity by non-linear FE analysis methods, Recommended Practice No. DNV-RP-C208*, Det Norske Veritas GL AS, Oslo, 2013, https://rules.dnv.com/docs/pdf/DNVPM/codes/docs/2013-06/RP-C208.pdf (accessed May 23, 2023).

35. ABUBAKAR A., DOW R.S., Simulation of ship grounding damage using the finite element method, *International Journal of Solids and Structures*, **50**(5): 623–636, 2013, https://doi.org/10.1016/j.ijsolstr.2012.10.016.

36. ALSOS H.S., AMDAHL J., On the resistance to penetration of stiffened plates, Part I – Experiments, *International Journal of Impact Engineering*, **36**(6): 799–807, 2009, https://doi.org/10.1016/j.ijimpeng.2008.10.005.

37. COWPER G.R., SYMONDS P.S., *Strain-hardening and strain-rate effects in the impact 11 loading of cantilever beams*, Technical report, C11, no. 28; C11/28, Brown University, Division of Applied Mathematics, Providence R.I., 1957, https://apps.dtic.mil/sti/pdfs/AD0144762.pdf (accessed May 23, 2023).

38. WANG C., CORBETT J.J., The costs and benefits of reducing SO_2 emissions from ships in the US West Coastal waters, *Transportation Research Part D: Transport and Environment*, **12**(8): 577–588, 2007, https://doi.org/10.1016/j.trd.2007.08.003.

39. ALSOS H.S., AMDAHL J., HOPPERSTAD O.S., On the resistance to penetration of stiffened plates, Part II: Numerical analysis, *International Journal of Impact Engineering*, **36**(7): 875–887, 2009, https://doi.org/10.1016/j.ijimpeng.2008.11.004.

40. WANG Z., HU Z., LIU K., CHEN G., Application of a material model based on the Johnson-Cook and Gurson-Tvergaard-Needleman model in ship collision and grounding simulations, *Ocean Engineering*, **205**: 106768, 2020, https://doi.org/10.1016/j.oceaneng.2019.106768.

41. Woelke P.B., Shields M.D., Abboud N.N., Hutchinson J.W., Simulations of ductile fracture in an idealized ship grounding scenario using phenomenological damage and cohesive zone models, *Computational Materials Science*, **80**: 79–95, 2013, https://doi.org/10.1016/j.commatsci.2013.04.009.

42. Lee S.-G., Lee J.-S., Lee H.-S., Park J.-H., Jung T.-Y., Full-scale ship collision, grounding and sinking simulation using highly advanced M&S system of FSI analysis technique, *Procedia Engineering*, **173**: 1507–1514, 2017, https://doi.org/10.1016/j.proeng.2016.12.232.

43. Pineau J.-P., Conti F., Le Sourne H., Looten T., A fast simulation tool for ship grounding damage analysis, *Ocean Engineering*, **262**: 112248, 2022, https://doi.org/10.1016/j.oceaneng.2022.112248.

44. Champley K.M., Willey T.M., Kim H., Bond K., Glenn S.M., Smith J.A., Kallman J.S., Brown W.D., Seetho I.M., Keene L., Azevedo S.G., McMichael L.D., Overturf G., Martz H.E., Livermore tomography tools: accurate, fast, and flexible software for tomographic science, *NDT & E International*, **126**: 102595, 2022, https://doi.org/10.1016/j.ndteint.2021.102595.

45. Wang G., Tamura K., Jiang D., Zhou Q.J., *Design Against Contact Damage for Offshore Supply Vessels*, ABS Technical Papers, 2006, https://superfloats.com/wp-content/uploads/2020/02/Design-Against-Contact-Damage-Offshore.pdf.

46. Prabowo A.R., Cao B., Sohn J.M., Bae D.M., Crashworthiness assessment of thin-walled double bottom tanker: Influences of seabed to structural damage and damage-energy formulae for grounding damage calculations, *Journal of Ocean Engineering and Science*, **5**(4): 387–400, 2020, https://doi.org/10.1016/j.joes.2020.03.002.

47. Wierzbicki T., Petalling of plates under explosive and impact loading, *International Journal of Impact Engineering*, **22**(9–10): 935–954, 1999, https://doi.org/10.1016/S0734-743X(99)00028-7.

48. Feng L., Hu L., Chen X., Shi H., A parametric study on effects of pitting corrosion on stiffened panels' ultimate strength, *International Journal of Naval Architecture and Ocean Engineering*, **12**: 699–710, 2020, https://doi.org/10.1016/j.ijnaoe.2020.08.001.

49. Wang R., On the effect of pit shape on pitted plates, Part II: Compressive behavior due to random pitting corrosion, *Ocean Engineering*, **236**: 108737, 2021, https://doi.org/10.1016/j.oceaneng.2021.108737.

50. Yang Y., Yu Q., He Z., Ma J., Qin J., Investigation on failure mechanism of stiffened plates with pitting corrosion under uniaxial compression, *Applied Ocean Research*, **102**: 102318, 2020, https://doi.org/10.1016/j.apor.2020.102318.